field approaches the Y axis, the resolution of the data was not sufficient to confirm all of the details beyond doubt. Therefore, more precise measurements were made on the spectrum of the lithium C nuclei neighboring the V_K center in LiF. The spin Hamiltonian diagonalization predicts a complicated angular dependence as the magnetic field is rotated about the Y axis into coincidence with the X axis. In particular, for the R_2 ESR line, the ENDOR lines cross before reaching the X axis and then come together again on the axis.

In Fig. 16, the R_2 ENDOR angular dependence calculated using the experimentally determined hyperfine constants is compared with carefully measured ENDOR line positions in the vicinity of the X axis. This confirms the details predicted by the diagonalization of the spin Hamiltonian.

PHYSICAL REVIEW VOLUME 175, NUMBER 2 10 NOVEMBER 1968

Electron-Nuclear Double-Resonance Study of the Self-Trapped Hole Associated with Lithium in NaF* †

ISAAC L. BASS

Department of Physics, Stanford University, Stanford, California

AND

ROBERT LEE MIEHER‡

Department of Physics, Purdue University, Lafayette, Indiana 47907

(Received 18 March 1968)

A new ESR center has been produced in NaF crystals containing lithium impurities by producing V_K centers and warming the crystal to 150°K so that the self-trapped holes can migrate until they associate with the impurities. The complex consisting of the self-trapped hole associated with a Li^+ impurity ion has been named the "V_{KA} center." The ESR spectrum can be interpreted in terms of a "bent-bond" F_2^- molecule ion. An electron-nuclear double-resonance (ENDOR) study of the V_{KA} center has provided definite confirmation of the assumed model. The difference in the ENDOR spectra of different ESR lines has been explained by a diagonalization of the complete spin Hamiltonian matrix which includes the hyperfine interactions of the unpaired electron with both the molecular nuclei and the lattice nuclei.

I. INTRODUCTION

THIS paper presents the results of electron-spin-resonance (ESR) and electron-nuclear double-resonance (ENDOR) studies of self-trapped holes (V_K centers) in NaF associated with lithium impurities. The name "V_{KA} center"[1] will be used to designate this associated center.

The ESR[2–5] and optical[6,7] properties of the self-trapped holes have been investigated in several alkali halides. Also, ENDOR studies of the V_K center have been carried out in LiF [8,9] and NaF.[10] All of the experiments have been successfully explained by the molecule-ion model in which the hole is shared by two adjacent halide ions to form a negatively charged diatomic molecule, e.g., F_2^-, oriented along a [110] crystalline direction. The association of the V_K center with the lithium impurity produces changes in the ESR spectrum which are similar to those described by Känzig[11] for the V_F center in LiF.

The experimental apparatus and the production of the V_{KA} centers are discussed in Sec. II. The ESR spectrum of the V_{KA} center is analyzed in Sec. III and compared with other V_K type centers. The ENDOR results that provide the positive identification of the geometry of the V_{KA} center are reported in Sec. IV. The ENDOR of the V_{KA} center is compared with the ENDOR of the unassociated V_K center in NaF [10] and LiF [8,9] and the

* Work supported by the National Science Foundation under Grant Nos. NSF-GP-3385 at Columbia University and NSF-GP-4680 at Purdue University.

† Partially based upon a thesis submitted by I. L. Bass for the Ph.D. degree at Columbia University.

‡ Alfred P. Sloan Foundation Fellow.

[1] I. L. Bass and R. Mieher, Phys. Rev. Letters **15**, 25 (1965).

[2] T. G. Castner and W. Kanzig, J. Phys. Chem. Solids **3**, 178 (1957).

[3] T. O. Woodruff and W. Kanzig, J. Phys. Chem. Solids **5**, 268 (1958).

[4] C. E. Bailey, Phys. Rev. **136**, A1311 (1964).

[5] C. P. Slichter, *Principles of Magnetic Resonance* (Harper and Row, Inc., New York, 1963).

[6] C. J. Delbecq, B. Smaller, and P. H. Yuster, Phys. Rev. **111**, 1235 (1958).

[7] C. J. Delbecq, W. Hayes, and P. H. Yuster, Phys. Rev. **121**, 1043 (1961).

[8] R. Gazzinelli and R. Mieher, Phys. Rev. Letters **12**, 644 (1964).

[9] R. Gazzinelli and R. Mieher, first preceding paper, Phys. Rev. **175**, 395 (1968).

[10] D. F. Daly and R. L. Mieher, preceding paper, Phys. Rev. **175**, 412 (1968).

[11] W. Känzig, Phys. Rev. Letters **4**, 117 (1960); J. Phys. Chem. Solids **17**, 80 (1960).

reader is referred to the two preceding papers for additional details of the isolated V_K centers.

II. EXPERIMENTAL

The ESR and ENDOR data were taken with an X-band, superheterodyne spectrometer. This spectrometer was similar to the one described in detail by Gazzinelli and Mieher.[9]

The samples were crystals of NaF grown from a melt containing about 1% of LiF. The crystals were grown by the Bridgman technique of lowering the molten salt through a thermal gradient. The salt was contained in high-purity graphite crucibles located on top of a hollow, water-cooled stainless-steel lowering rod. The crucible was in a stainless-steel vacuum tube in a vertical two-zone furnace. The lowering rod moved through a vacuum seal.

The system was first baked out at a temperature about 100°C below the melting point of the salt and during crystal growth there was a continuous flow of dry argon through the system.

Those samples for which the magnetic field was rotated in a (100) plane were cleaved from the boule along the (100) cleavage planes. Typical sample dimensions are approximately $\frac{7}{32}\times\frac{7}{32}\times\frac{1}{2}$ in. The samples for which the magnetic field was rotated in a (110) plane have similar dimensions. The rotation axis, which is parallel to the $\frac{1}{2}$-in. edges of the sample is a [110] crystalline direction. Two of the long lateral faces are cleaved (100) planes. The other two lateral faces and the two end faces are all (110) planes which were ground and polished within a tolerance of $\sim 1°$ or better.

Production of the V_{KA} centers for ESR and ENDOR studies is done as follows. After mounting in the spectrometer and cooling to liquid-N_2 temperature, the samples are irradiated for about 24 h with the x-ray tube set at 75 kV and 30 mA. The x-ray equipment used is the same as that described by Gazzinelli and Mieher.[9] After irradiation, the sample is protected from exposure to light by the microwave cavity or a light shield. The sample is then warmed by blowing the liquid-N_2 out of the coolant container to which it is attached. The temperature is monitored by a copper-constantan thermocouple attached to the bottom of this container. The onset of conversion of V_K centers to V_{KA} centers is observed at 140°K, and the conversion is complete at 160°K. The V_{KA} centers are stable at 160°K. The conversion can be monitored by observing the ESR of the V_K and V_{KA} centers.

The conversion efficiency based on ESR amplitude ratios appears to be near 100%. Attempts were made to orient the V_{KA} centers by optical methods that were successfully used to orient V_K centers in NaF and LiF. However, the V_{KA} centers were disassociated with a consequent regeneration of V_K centers.

The coolant container is refilled with liquid N_2 and the sample is kept at that temperature or lower for the duration of the experiment. The optimum signal to noise for the ENDOR studies is obtained with liquid H_2 as the coolant. The sample temprature was about 40°K because of exposure to room-temperature radiation.

III. ESR SPECTRUM

A. Qualitative Picture

The ESR spectrum of the lithium V_{KA} center in NaF is similar to that of the V_K centers in the alkali fluorides[2–4] and that of the V_F center in LiF.[11] The total spectrum observed is a superposition of the spectra produced by the six different orientations of V_{KA} centers corresponding to the six [110] lattice directions. They exhibit the large resolved anisotropic hyperfine interaction of the two molecular nuclei that is characteristic of all the V_K type centers observed in halide salts. The hyperfine interactions of the lattice nuclei surrounding the molecule ion are not resolved in ESR but produce an inhomogeneously broadened line whose width is ≈ 9 G for the lithium V_{KA} center in NaF. The effective ESR spin Hamiltonian of the V_{KA} center is the one used by Känzig for the V_F center[11] which is applicable to any bent-bond V_K center. It is given by

$$\mathcal{H}_{ESR}/g_0\beta_0=\mathbf{H}_0\cdot\mathbf{g}/g_0\cdot\mathbf{S}+\mathbf{K}_1\cdot\mathbf{T}_1\cdot\mathbf{S}+\mathbf{K}_2\cdot\mathbf{T}_2\cdot\mathbf{S}-(\gamma_F h/g_0\beta_0)(\mathbf{K}_1+\mathbf{K}_2)\cdot\mathbf{H}_0, \quad (1)$$

where $\mathbf{H}_0$ is the dc magnetic field, S is the electron spin operator, $S=\frac{1}{2}$, $\mathbf{g}$ is the electronic g tensor; $\mathbf{K}_1$ and $\mathbf{K}_2$ are the spin operators of the molecular fluorine nuclei, $K_1=K_2=\frac{1}{2}$, $\mathbf{T}_1$ and $\mathbf{T}_2$ are the hyperfine tensors of the molecular fluorine nuclei, g_0 is the free-electron g factor=

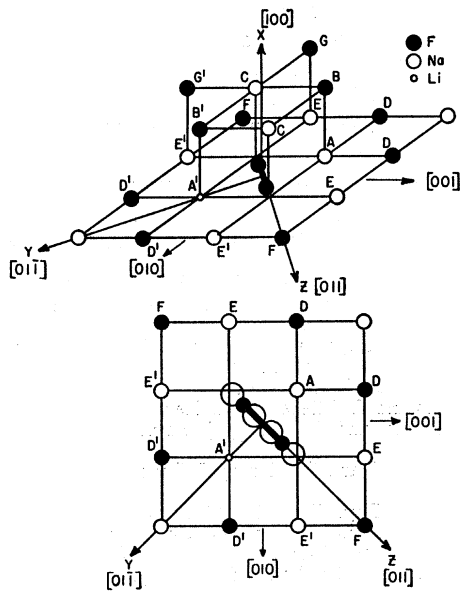

FIG. 1. Geometry of the lithium V_{KA} center and lettering of nearby lattice nuclei.

TABLE I. Principal values of the g tensors, principal values of the molecular-fluorine hyperfine tensors (in G), and the bond angles (δ) of the lithium V_{KA} center and the V_K center in NaF, and of the V_F center and V_K center in LiF.

Crystal	Center	g_x	g_y	g_z	$\lvert T_x \rvert$ (G)	$\lvert T_y \rvert$ (G)	T_z (G)	δ
NaF	Li V_{KA}	2.0219±0.0002	2.0231±0.0002	2.0020±0.0001	<7	<7	916.4(+0.3, −0.1)	0.6±0.2°
	V_K[a]	2.0220	2.0220	2.0014	47	47	897.1	
LiF	V_F[b]	2.023±0.002	2.023±0.002	2.001±0.002	≈0	≈0	915	≈4°
	V_K[a]	2.0239	2.0239	2.0034	57	57	883.7	

[a] Reference 4. [b] Reference 11.

2.0023; β_0 is the Bohr magneton, γ_F is the fluorine nuclear gyromagnetic ratio; and h is Planck's constant.

The geometry of the V_{KA} center is shown in Fig. 1. Figure 2 shows the orientations of the principal axes x_1, y_1, and z_1, and x_2, y_2, and z_2 of the hyperfine tensors $\mathbf{T}_1$ and $\mathbf{T}_2$ relative to the principal axes X, Y, and Z of the tensor $\mathbf{g}$ and of the electron distribution of the molecule ion. The angle δ by which the principal axes of the hyperfine tensors are rotated with respect to the XYZ coordinates is defined as the bond angle. The hyperfine tensors of all the V_K centers observed in the alkali halides,[2–4] as well as those of the V_F center in LiF [11] and of the lithium V_{KA} center in NaF, have been found to be axially symmetric about their respective z axes within experimental error. The parallel principal value T_z is typically 900 G for all the F_2^- centers,[3,4,11] while the perpendicular principal values T_x and T_y range from 30 to 60 G for the F_2^- V_K centers[3,4] and are approximately 0 G for the two bent-bond F_2^- centers (the V_F and V_{KA}). The principal values of the hyperfine tensors $\mathbf{T}_1$ and $\mathbf{T}_2$, the principal values of $\mathbf{g}$, and the bond angle δ are compared in Table I for the V_K center and the lithium V_{KA} center in NaF, and for the V_K center and V_F center in LiF.

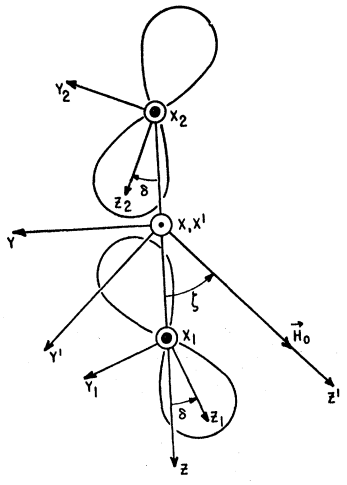

FIG. 2. Orientation of the principal axes of the molecular fluorine hyperfine tensors relative to the XYZ principal axes of the V_{KA} center. The figure eights indicate the distortion of the σ_u molecular orbital due to the bent bond. The x', y', z' axes rotate with the magnetic field.

The F_2^- molecule ion in a lattice, whether bent bond or not, generally produces four ESR lines corresponding to the four independent spin states of the two spin-$\frac{1}{2}$ molecular fluorine nuclei. These states may be classified by the projection quantum number $M=\pm1, 0, 0$, of the total nuclear spin $\mathbf{K}^+=\mathbf{K}_1+\mathbf{K}_2$ along the internuclear axis (the superscript + is used because the operator $\mathbf{K}^-=\mathbf{K}_1-\mathbf{K}_2$ will be introduced later). The angular dependence of the four ESR lines of the V_K center and of the lithium V_{KA} center in NaF is shown in Fig. 3 for rotation of the magnetic field in planes containing the molecular axis. The ordinate ζ is the angle between the magnetic field and the molecular axis. The lines are designated by both the conventional labels, R_1, R_2, R_3, and R_4 [3] and by (±1), (0), which denotes the corresponding value of M.

Although there is an over-all similarity in the spectra of the two centers, the R_2 and R_3 lines of the V_{KA} center are resolved in the range ≈20°–75°, where they are unresolved for the V_K center. This splitting is the principal difference between the ESR spectra of an F_2^- V_K center and an F_2^- bent-bond center. It occurs to some extent for all field orientations where the molecular fluorines of the bent-bond center are nonequivalent. Thus the splitting is greatest for field rotation in the YZ, plane as in Fig. 3, and is zero for field rotation in the XZ plane. The splitting is linear in δ for a given orientation of magnetic field (see quantitative discussion to follow). Känzig[11] noted these basic differences between the ESR spectra of the V_K center and the bent-bond V_K center when he observed them in the V_F center in LiF.

Since the bond angle of the V_{KA} center is substantially less than that of the V_F center (see Table I), the splitting of the R_2 and R_3 lines is correspondingly less. Clear-cut observations of these splittings were consequently hindered for most orientations of magnetic field by overlap of the R_2, R_3, and R_4 lines of different orientations of V_{KA} centers. Nevertheless, four different orientations of centers become equivalent when the field is parallel to a [100] or a [110] direction, and the splitting of the R_2 and R_3 lines of these centers is readily discerned in each instance. The ESR spectra of the V_{KA} center for these two field orientations are shown in Fig. 4 and are compared with the corresponding spectra of the V_K center in NaF in Fig. 5. The splitting of the $R_2(45°)$ and $R_3(45°)$ lines for $\mathbf{H}_0$ parallel to [100], and of the $R_2(60°)$

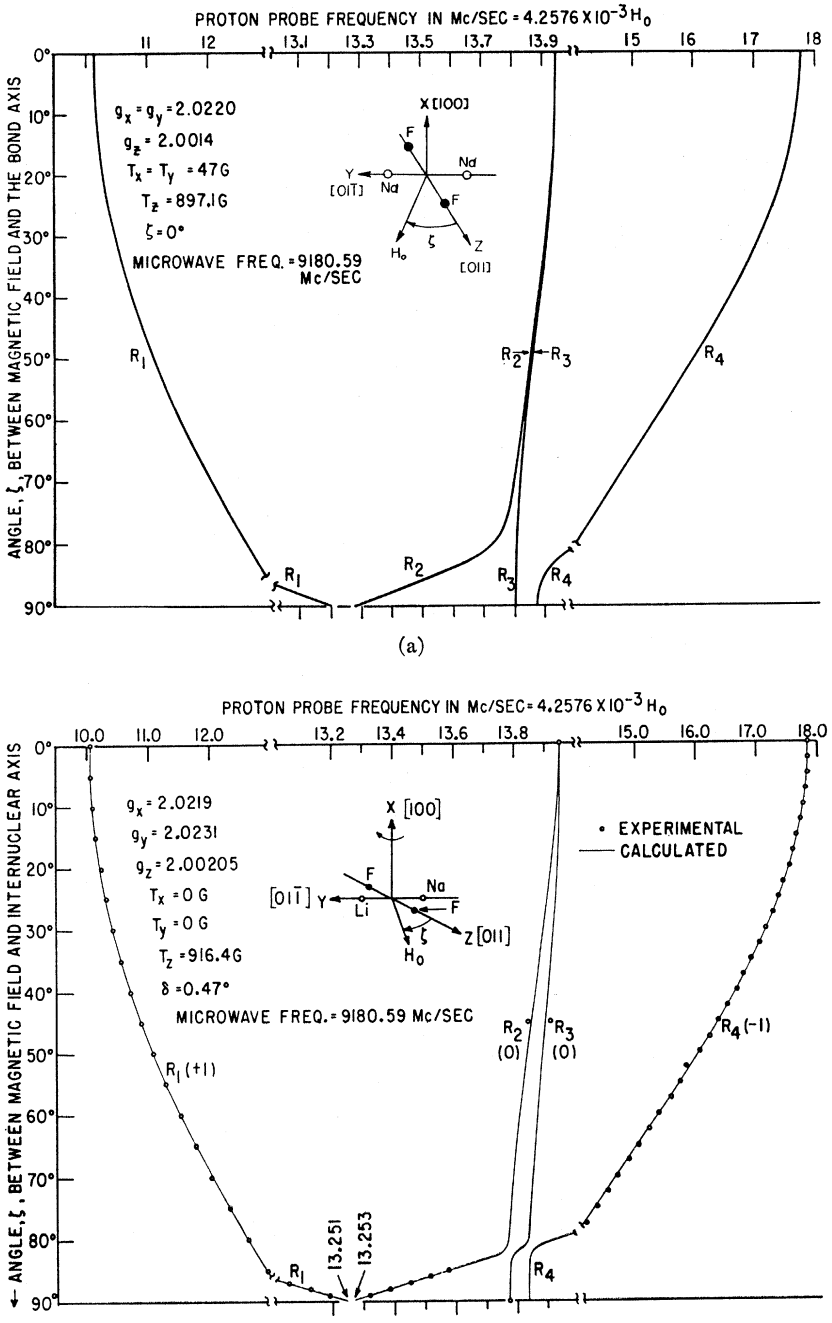

FIG. 3. (a) Angular dependence of the ESR of the V_K center in NaF as calculated by matrix diagonalization; (b) angular dependence of the ESR of the lithium V_{KA} center in NaF. The value of δ is chosen so that theory and experiment agree for the R_3 line for $\zeta = 90°$.

and $R_3(60°)$ lines for $\mathbf{H}_0$ parallel to [110], are clearly evident even though they overlap the R_2, R_3, and R_4 lines of the other two orientations of V_{KA} centers. Although there is no evidence to the contrary, a definite confirmation of the degeneracy of the R_2 and R_3 lines when the field is contained in the XZ plane of the V_{KA} center was not possible for the reasons mentioned above.

B. Quantitative Analysis and Experimental Results

The ESR data were analyzed by numerical diagonalization of the matrix of the spin Hamiltonian in Eq. (1). An IBM 7090 computer was used for the calculations. Similar matrix diagonalization methods were used by Woodruff and Kanzig[3] and by Bailey[4] for the V_K centers in various alkali fluorides. The analytic form of the matrix used in the present calculation (Table II) is applicable to any F_2^- bent-bond center for field rotations in the YZ plane, includes the Zeeman interaction of the molecular fluorines, and imposes no restrictions on the symmetries of the tensors $\mathbf{T}_1$ and $\mathbf{T}_2$, and $\mathbf{g}$. The matrix becomes identical to the one used previously for the V_K centers[3,4] if the bond angle δ is set to zero, the fluorine

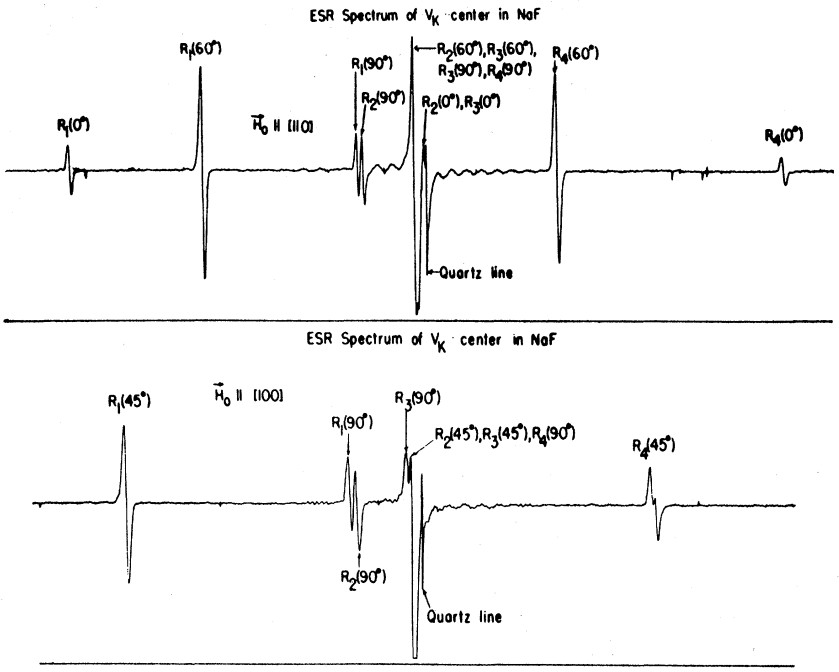

FIG. 4. The ESR spectra of the V_K center in NaF before conversion to the V_{KA} center. The top recorder trace is for H_0 parallel to [110] and the bottom trace for H_0 parallel to [100]. Splitting of the $R_4(45°)$ line is caused by slight crystal misorientation.

Zeeman terms are dropped, and $\mathbf{g}$, $\mathbf{T}_1$, and $\mathbf{T}_2$ are assumed to be axially symmetric about their respective z axes, i.e., $g_X = g_Y$ and $T_x = T_y$. The calculations eventually showed that incorporation of the bond angle δ into the V_K center matrix was actually the only additional feature essential for the analysis of the V_{KA} center data. Limitation of field rotation to the YZ plane simplifies the algebraic expressions and the calculations but does not prevent accurate determination of the Hamiltonian parameters.

In deriving the matrix of Table II, the ESR Hamiltonian is written as the sum of an expression almost identical with the V_K center Hamiltonian and some terms which represent the effects of the bent bond. The molecular nuclei of the V_K center are equivalent, and it is possible to eliminate $\mathbf{K}_1$ and $\mathbf{K}_2$ from its ESR Hamiltonian by the substitution $\mathbf{K}^+ = \mathbf{K}_1 + \mathbf{K}_2$ as has been done previously.[2,3] For the sake of comparison it is desirable to use $\mathbf{K}^+$ in the bent-bond Hamiltonian as well, but the nonequivalence of the molecular nuclei

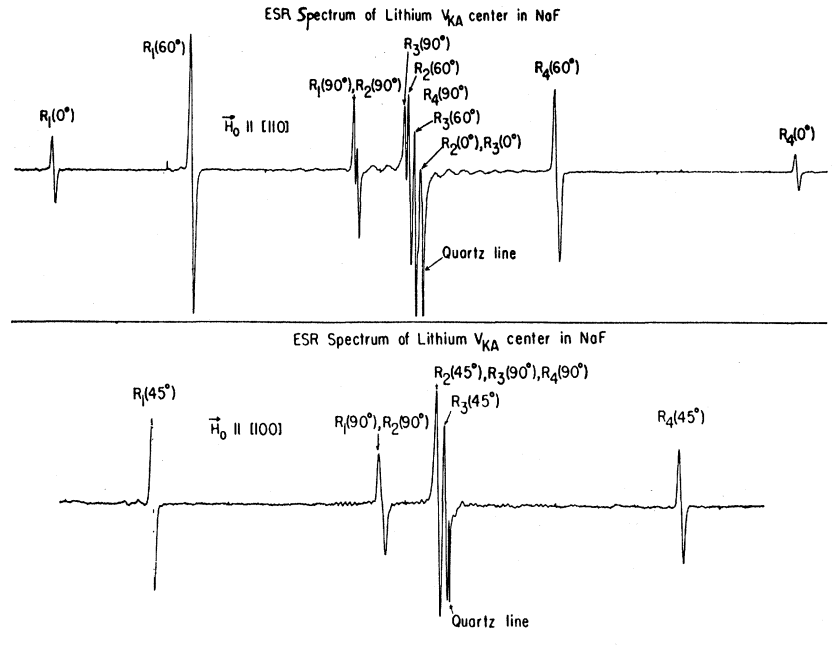

FIG. 5. The ESR spectra of the lithium V_{KA} center in NaF. The top recorder trace is for H_0 parallel to [110] and the bottom trace for H_0 parallel to [100]. Splitting of the $R_1(90°)$ and $R_2(90°)$ line in the top trace is caused by slight crystal misorientation.

TABLE II. The matrix $\langle m_s, K^+, M \mid \mathcal{H}_{ESR} \mid m_s', K^{+\prime}, M' \rangle$. The states $\mid 1\rangle$, $\mid 2\rangle$, etc., are given in Eq. (8) and the terms A, B, C, etc., are given in Eq. (9).

$\mid 1\rangle$	$\mid 2\rangle$	$\mid 3\rangle$	$\mid 4\rangle$	$\mid 5\rangle$	$\mid 6\rangle$	$\mid 7\rangle$	$\mid 8\rangle$	
$A-B+C$	$D-E$	0	$-F$	$G+H$	$-I+J$	0	$-K$	$\langle 1 \mid$
	A	$D-E$	$-K\sqrt{2}$	$I+J$	G	$-I+J$	$F\sqrt{2}$	$\langle 2 \mid$
		$A+B-C$	F	0	$I+J$	$G-H$	K	$\langle 3 \mid$
			A	$-K$	$F\sqrt{2}$	K	G	$\langle 4 \mid$
				$-A-B-C$	$D+E$	0	F	$\langle 5 \mid$
					$-A$	$D+E$	$K\sqrt{2}$	$\langle 6 \mid$
						$-A+B+C$	$-F$	$\langle 7 \mid$
							$-A$	$\langle 8 \mid$

prevents a complete elimination of $\mathbf{K}_1$ and $\mathbf{K}_2$ in this fashion. It was found that if the additional relation $\mathbf{K}^-=\mathbf{K}_1-\mathbf{K}_2$ is introduced, the V_K center part of the ESR Hamiltonian is expressed in terms of $\mathbf{K}^+$ only, the bent-bond part in terms of $\mathbf{K}^-$ only, and $\mathbf{K}_1$ and $\mathbf{K}_2$ no longer appear.

The quantization directions of the spin operators and the zeroth-order spin functions are the same as those used in the previous V_K center calculations.[3] The electron spin $\mathbf{S}$ is quantized along the magnetic field or the z' axis in Fig. 2. The spin operators $\mathbf{K}^+$ and $\mathbf{K}^-$, or equivalently, $\mathbf{K}_1$ and $\mathbf{K}_2$, are quantized along the molecular or Z axis. The eight basis spin functions are taken to be the product states,

$$\mid m_s\rangle \mid K^+, M\rangle = \mid m_s, K^+, M\rangle, \tag{2}$$

where

$$m_s=\pm\tfrac{1}{2},$$

$$K^+=1, 0,$$

and

$$M=\pm 1, 0.$$

The quantum number m_s is the projection of $\mathbf{S}$ along $\mathbf{H}_0$, $\mathbf{K}^+$ is the total nuclear spin of the molecule ion in the singlet-triplet representation, and M is the projection quantum number of $\mathbf{K}^+$ along the Z axis. The expressions for the combined nuclear spin functions $\mid K^+, M\rangle$, in terms of the spin functions $\mid K_i, M_i\rangle_i$, $i=1, 2$, of the ith molecular nucleus, are

$$\begin{aligned}
&\mid 1, 1\rangle = \mid \tfrac{1}{2}, \tfrac{1}{2}\rangle_1 \mid \tfrac{1}{2}, \tfrac{1}{2}\rangle_2,\\
&\mid 1, 0\rangle = \tfrac{1}{2}\sqrt{2}(\mid \tfrac{1}{2}, \tfrac{1}{2}\rangle_1 \mid \tfrac{1}{2}, -\tfrac{1}{2}\rangle_2 + \mid \tfrac{1}{2}, -\tfrac{1}{2}\rangle_1 \mid \tfrac{1}{2}, \tfrac{1}{2}\rangle_2),\\
&\mid 1, -1\rangle = \mid \tfrac{1}{2}, -\tfrac{1}{2}\rangle_1 \mid \tfrac{1}{2}, -\tfrac{1}{2}\rangle_2,\\
&\mid 0, 0\rangle = \tfrac{1}{2}\sqrt{2}(\mid \tfrac{1}{2}, \tfrac{1}{2}\rangle_1 \mid \tfrac{1}{2}, -\tfrac{1}{2}\rangle_2 - \mid \tfrac{1}{2}, -\tfrac{1}{2}\rangle_1 \mid \tfrac{1}{2}, \tfrac{1}{2}\rangle_2).
\end{aligned} \tag{3}$$

In order to calculate the analytic form of the matrix in the chosen representation, the ESR Hamiltonian is expanded with the components of $\mathbf{S}$ expressed in the $x'y'z'$ coordinate system and the components of $\mathbf{K}^+$ and $\mathbf{K}^-$ expressed in the XYZ coordinate system (Fig. 2). Each term is first expanded in the principal-axis coordinate system of the tensor involved. This gives

$$\begin{aligned}
\mathcal{H}_{ESR}/g_0\beta_0 = {}& (g_Z/g_0) H_0 S_Z \cos\zeta - (g_Y/g_0) H_0 S_Y \sin\zeta\\
&+ T_x K_{1,x_1} S_{x_1} + T_y K_{1,y_1} S_{y_1} + T_z K_{1,z_1}, S_{z_1}\\
&+ T_x K_{2,x_2} S_{x_2} + T_y K_{2,y_2} S_{y_2} + T_z K_{2,z_2} S_{z_2}\\
&- (H\gamma_F/g_0\beta_0) K_{z'}{}^+ + H_0.
\end{aligned} \tag{4}$$

A counterclockwise rotation by an angle α about one of the x axes in Fig. 2 is given by

$$R(\alpha) = \begin{vmatrix} 1 & 0 & 0 \\ 0 & \cos\alpha & \sin\alpha \\ 0 & -\sin\alpha & \cos\alpha \end{vmatrix}. \tag{5}$$

By use of the transformations

$$\begin{aligned}
S_{X,Y,Z} &= R(-\zeta) S_{x'y'z'},\\
S_{x_1y_1z_1} &= R(-\zeta+\delta) S_{x'y'z'},\\
S_{x_2y_2z_2} &= R(-\zeta-\delta) S_{x'y'x'},\\
K_{1,x_1y_1z_1} &= R(\delta) K_{1,XYZ},\\
K_{2,x_2y_2z_2} &= R(-\delta) K_{2,XYZ},\\
K_{z'}{}^+ &= -K_Y{}^+ \sin\zeta + K_Z{}^+ \cos\zeta,
\end{aligned} \tag{6}$$

Eq. (4) can be written in the desired form,

$$\begin{aligned}
\mathcal{H}_{ESR}/g_0\beta_0 = {}& (H_0/g_0)(g_z \cos^2\zeta + g_Y \sin^2\zeta) S_{z'}\\
&+ (H_0/g_0)(g_z - g_Y)(\sin\zeta\cos\zeta) S_{y'}\\
&+ T_x K_X{}^+ S_{x'}\\
&+ T_{yz} K_Y{}^+ (S_{y'}\cos\zeta - S_{z'}\sin\zeta)\\
&+ T_{zy} K_Z{}^+ (S_{y'}\sin\zeta + S_{z'}\cos\zeta)\\
&+ \Delta T_{yz} K_Y{}^- (S_{y'}\sin\zeta + S_{z'}\cos\zeta)\\
&+ \Delta T_{yz} K_Z{}^- (S_{y'}\cos\zeta - S_{z'}\sin\zeta)\\
&+ (h\gamma_F/g_0\beta_0)(H_0\sin\zeta) K_Y{}^+\\
&- (h\gamma_F/g_0\beta_0)(H_0\cos\zeta) K_Z{}^+,
\end{aligned} \tag{7}$$

where

$$T_{yz}=T_y\cos^2\delta+T_z\sin^2\delta,$$
$$T_{zy}=T_y\sin^2\delta+T_z\cos^2\delta,$$
$$\Delta T_{yz}=(T_y-T_z)\sin\delta\cos\delta.$$

The matrix $\langle m_s, K^+, M \mid \mathcal{H}_{\rm ESR} \mid m_s', K^{+\prime}, M'\rangle$ is given in Table II. The states $\langle\mid m_s, K^+, M \mid$ are represented by

$$\begin{aligned}
\langle 1 \mid &= \langle \tfrac{1}{2}, 1, 1 \mid,\\
\langle 2 \mid &= \langle \tfrac{1}{2}, 1, 0 \mid,\\
\langle 3 \mid &= \langle \tfrac{1}{2}, 1, -1 \mid,\\
\langle 4 \mid &= \langle \tfrac{1}{2}, 0, 0 \mid,\\
\langle 5 \mid &= \langle -\tfrac{1}{2}, 1, 1 \mid,\\
\langle 6 \mid &= \langle -\tfrac{1}{2}, 1, 0 \mid,\\
\langle 7 \mid &= \langle -\tfrac{1}{2}, 1, -1 \mid,\\
\langle 8 \mid &= \langle -\tfrac{1}{2}, 0, 0 \mid.
\end{aligned} \tag{8}$$

The terms A, B, C, etc., are

$$\begin{aligned}
A&=(U_0H_0/2g_0)(g_Z\cos^2\zeta+g_Y\sin^2\zeta),\\
B&=\gamma_F H_0\cos\zeta,\\
C&=\tfrac{1}{2}U_0T_{zy},\\
D&=(\gamma_F H_0/\sqrt{2})\sin\zeta,\\
E&=(U_0T_{zy}/2\sqrt{2})\sin\zeta,\\
F&=(U_0\Delta T_{yz}/2\sqrt{2})\cos\zeta,\\
G&=(U_0H_0/2g_0)(g_Z-g_Y)\sin\zeta\cos\zeta,\\
H&=\tfrac{1}{2}(U_0T_{zy})\sin\zeta,\\
I&=U_0T_x/2\sqrt{2},\\
J&=(U_0T_{yz}/2\sqrt{2})\cos\zeta,\\
K&=(U_0\Delta T_{yz}/2\sqrt{2})\sin\zeta,
\end{aligned} \tag{9}$$

where $U_0=10^{-6}\,g_0\beta_0/h$ and γ_F is in units of Mc sec^{-1}G^{-1}, so that all terms are in Mc/sec units. The submatrices such as

$$\langle K^+, M \mid K_j^+ \mid K^{+\prime}, M'\rangle$$

that were used to obtain Eq. (9) are discussed in the Appendix.

The computer program would first evaluate the ESR matrix for a given orientation and some arbitrary magnitude of magnetic field ($\approx$3000 G), compute its eigenvalues, and then calculate the frequency of a particular transition (R_1, R_2, R_3, or R_4) from these eigenvalues. The field magnitude was adjusted by iteration of these steps until the computed transition frequency and the fixed microwave frequency (9180.6 Mc/sec) agreed within 0.1 Mc/sec. The computed results were expressed as proton probe frequencies for direct comparison with the experimentally measured proton probe frequency. Angular dependences and ESR line positions [Fig. 3(b) and Table III] could be computed in this fashion for a particular set of ESR parameters.

The parameters g_X, g_Y, g_Z, T_x, T_y, T_z, and δ of the lithium V_{KA} center in NaF are determined as follows:

(1) g_Z is determined by the R_3 line position when $\mathbf{H}_0$ is parallel to the Z axis, i.e., the $R_3(0°)$ line with $\mathbf{H}_0 \parallel [110]$ (Fig. 5);

(2) T_z is determined by the separation of the R_1 and R_4 lines when $\mathbf{H}_0$ is parallel to the Z axis, i.e., the $R_1(0°)$ and $R_4(0°)$ lines with $H_0 \parallel [110]$ (Fig. 5);

(3) g_X and g_Y are determined by the R_2 line position when $\mathbf{H}_0$ is parallel to the X and Y axes, respectively, i.e., the $R_2(90°)$ lines with $\mathbf{H}_0 \parallel [100]$ and $\mathbf{H}_0 \parallel [110]$, respectively (Fig. 5);

(4) T_x and T_y are determined by the separation of the R_1 and R_2 lines when $\mathbf{H}_0$ is parallel to the X and Y axes, respectively, i.e., the $R_1(90°)$ and $R_2(90°)$ lines with $\mathbf{H}_0 \parallel [100]$ and $\mathbf{H}_0 \parallel [110]$, respectively (Fig. 5);

(5a) δ is determined by the R_3 line position when $\mathbf{H}_0$ is parallel to the Y axis, i.e., the $R_3(90°)$ line when $\mathbf{H}_0 \parallel [110]$ (Fig. 5);

(5b) or δ is determined by the separation of the R_2 and R_3 lines when $\mathbf{H}_0$ is contained in the YZ plane and makes a 45° angle with the Z axis, i.e., the $R_2(45°)$ and $R_3(45°)$ lines with $\mathbf{H}_0 \parallel [100]$ (Fig. 5).

These measurements are similar to thoses used in the V_K center analysis,[3,4] but g_X and g_Y are determined from $R_2(90°)$ lines in this treatment whereas $g_\perp$ was determined from the $R_3(90°)$ line previously. The difference arises because the $R_3(90°)$ line position is significantly influenced by the bent bond. The method used to determine g_X and g_Y was justified by computer calculations which showed that the $R_2(90°)$ line position is independent, within experimental uncertainty, of T_x or T_y and δ. This feature of the 90° spectrum is illustrated in Fig. 6, which shows the dependence of line positions on various ESR parameters with $\mathbf{H}_0$ parallel to the Y axis. The dependence of the $R_3(90°)$ line position on δ permits the determination of this parameter by measurement (5a).

The magnetic field orientations required for the five measurements are all contained in a (100) crystalline plane. Thus, the crystal was rotated about a $\langle 100\rangle$ axis which was perpendicular to the field within an estimated uncertainty of $\approx$1°. The results of the measurements are contained in Table III. The difference between the positive and negative uncertainties in the positions of the $R_1(0°)$ and $R_4(0°)$ lines arises because any misorientation of the rotation axis decreases their separation. Measurements (3) and (4) required special methods because the $R_1(90°)$ and $R_2(90°)$ lines are not resolved and have a strong V-shaped angular dependence as the field is rotated through one of the [100] or [110] directions contained in the (100) plane of rotation [see Fig. 3(b)]. The line positions were

TABLE III. Calculated[a] and experimental line positions (proton frequency in Mc/sec) for magnetic field rotated in YZ plane of lithium V_{KA} center in NaF.

Angle		R_1 Line	R_2 Line	R_3 Line	R_4 Line
0°	Expt.	10.0471(+0.0015, −0.0005)	13.9488±0.0003	13.9488±0.0003	17.8509(−0.0015, +0.0005)
	Calc.	10.0469	13.9488	13.9488	17.8509
15°	Expt.	10.141±0.010			17.661±0.010
	Calc.	10.1380	13.9306	13.9473	17.6653
30°	Expt.	10.418±0.010			17.132±0.010
	Calc.	10.4117	13.8960	13.9282	17.1349
45°	Expt.	10.882±0.010	13.8384±0.0003	13.9146±0.0001	16.338±0.010
	Calc.	10.8683	13.8530	13.8983	16.3291
60°	Expt.	11.515±0.010			15.347±0.010
	Calc.	11.5044	13.8119	13.8670	15.3461
75°	Expt.	12.317±0.010			14.317±0.010
	Calc.	12.3080	13.7822	13.8433	14.2907
90°	Expt.	13.2510±0.0015	13.2528±0.0015	13.7737±0.0003	
	Calc.	13.2499	13.2525	13.7735	13.8367

[a] Parameters used in calculation are $T_x=T_y=0$, $T_z=916.4$ G, $\delta=0.47°$, $g_X=2.0219$, $g_Y=2.0231$, $g_Z=2.00205$, and $f_{MIC}=9180.59$ Mc/sec. Calculated proton frequencies are numerically accurate to ±0.1 kc/sec.

obtained by extrapolating the two branches of the V to their crossing point. The estimated uncertainty in these measurements is ≈1.5 kc/sec.

The ESR parameters obtained for the lithium V_{KA} center in NaF are given in Table I. The value of δ is an average of the values obtained by methods (5a) (0.47°) and (5b) (0.79°), and its uncertainty is determined by the discrepancy between the two values. With these parameters the entire angular dependence can be calculated and compared with the experimental angular dependence as in Fig. 3(b). A quantitative comparison is made in Table III, where calculated and experimental proton probe frequencies are listed for several specific field orientations. The line positions called for in measurements (1)–(5) were determined more carefully than the others and have correspondingly smaller uncertainties. The ±0.01 Mc/sec uncertainty of the latter measurements is a rough (probably excessive) estimate based on the scatter of experimental points about a smooth curve drawn to fit their angular dependence [Fig. 3(b)]. This estimate may not include some systematic error which, for example, may occur in the measured angle between the field and the molecular axis.

C. Description by Perturbation Theory

Many features of the ESR angular dependence of the F_2^- centers can be understood from a perturbation theory point of view. Most important for the V_{KA} and V_F centers of course is the splitting of the R_2 and R_3 lines(see Fig. 3) caused by the bent bond. These lines are produced by the two $M=0$ states of the molecular nuclei, namely, the singlet and $M=0$ component of the triplet. Inspection of the ESR Hamiltonian matrix (Table II) shows that for each of the electronic states ($m_s=\pm\frac{1}{2}$), the diagonal matrix elements associated with the $M=0$ nuclear states, $\langle\pm\frac{1}{2}, 1, 0 \mid \mathcal{H}_{\rm ESR} \mid \pm\frac{1}{2}, 1, 0\rangle$ and $\langle\pm\frac{1}{2}, 0, 0 \mid \mathcal{H}_{\rm ESR} \mid \pm\frac{1}{2}, 0, 0\rangle$, are degenerate in first order. They are also coupled directly by the matrix elements $\langle\pm\frac{1}{2}, 1, 0 \mid \mathcal{H}_{\rm ESR} \mid \pm\frac{1}{2}, 0, 0\rangle$. This matrix element vanishes when there is no bent bond or when the field is contained in the XZ plane of a bent-bond center

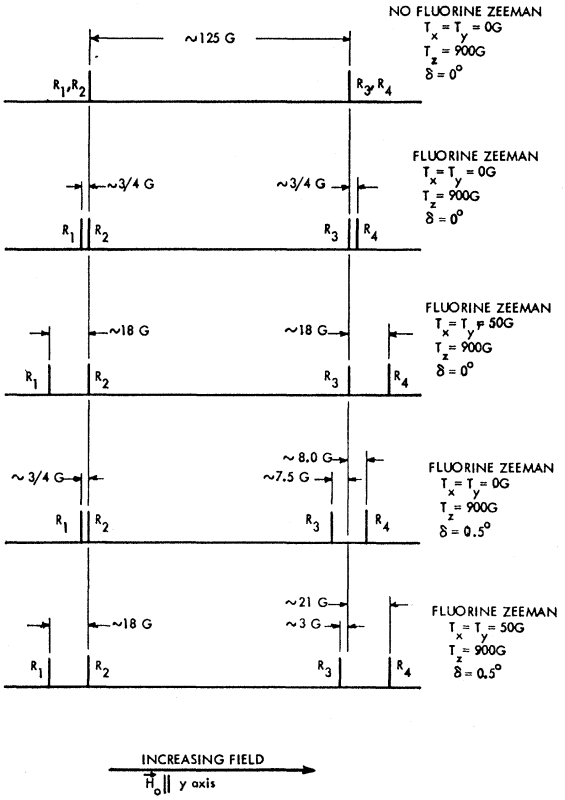

FIG. 6. The dependence of ESR spectra on molecular fluorine hyperfine parameters when the magnetic field is perpendicular to the F_2^- bond axis of the V_K or V_{KA} center. The term "fluorine Zeeman" indicates that the term $\gamma_F(K_1+K_2)\cdot H_0$ has been included in the Hamiltonian.

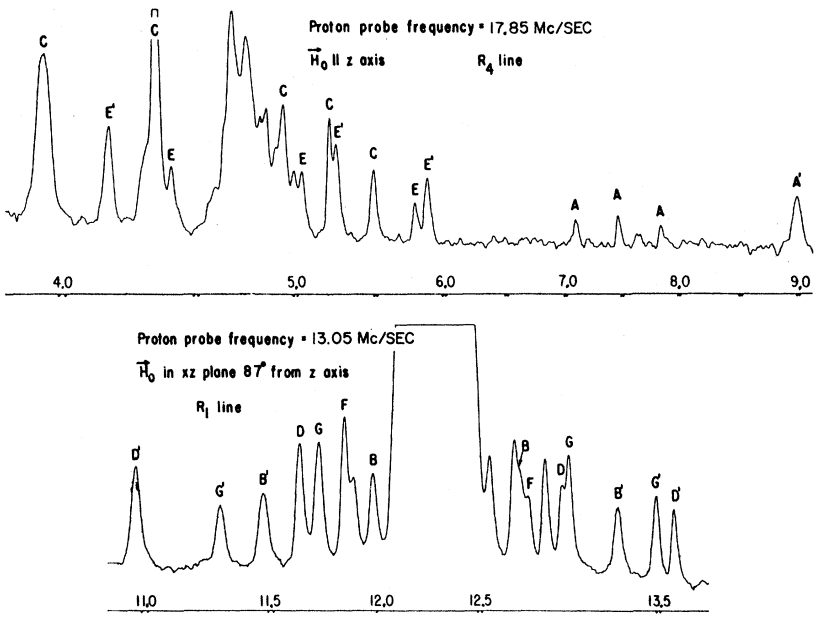

FIG. 7. Typical ENDOR recorder tracings of the lithium V_{KA} center in NaF.

(i.e., when the molecular nuclei are equivalent). When nonvanishing it produces a significant effect because the states it couples are degenerate. Application of degenerate perturbation theory gives a separation between the R_2 and R_3 lines of $(g_0/g)(T_z-T_y)\sin 2\delta \sin\zeta$ (G). This result is a good approximation up to $\zeta\approx 75°$ where other off-diagonal matrix elements begin to complicate the perturbation theory.

In the range $75°<\zeta\leq 90°$ the ESR spectrum does not exhibit the symmetry which is apparent for $\zeta<75°$, and it is no longer a good first-order approximation to associate the R_1 line with $M=+1$, the R_4 line with $M=-1$, and the R_2 and R_3 lines with $M=0$. At $\zeta=0°$ the R_1 and R_4 lines are centered on the R_2 and R_3 lines, but as ζ increases their center of gravity is shifted increasingly to lower fields than the R_2 and R_3 lines (neglecting the comparatively small splitting of the R_2 and R_3 lines caused by a bent bond) by the second-order perturbation of the matrix elements $\langle \frac{1}{2}, 1, \pm 1 \mid \mathcal{H}_{\mathrm{ESR}} \mid -\frac{1}{2}, 1, \pm 1\rangle$. As a result, the R_2 and R_4 lines would cross at $\zeta\approx 82°$ if their angular dependence curves for $\zeta<75°$ were extrapolated linearly to 90°. Instead they repel each other, a fact which is reminiscent of antilevel crossings in atoms. Indeed, there is a similar cause for both phenomena. Namely, energy levels which approach each other as some parameter is varied in the Hamiltonian (ζ in the F_2^- ESR Hamiltonian and the magnetic field in the atomic Hamiltonian) repel each other at their would be crossing point if they are coupled by off-diagonal matrix elements. For the typical F_2^- center, the energy levels involved in the R_4 transition, after being shifted by the second-order perturbations of $\langle \frac{1}{2}, 1, -1 \mid \mathcal{H}_{\mathrm{ESR}} \mid -\frac{1}{2}, 1, -1\rangle$, would cross the energy levels involved in the R_2 transition at $\zeta\approx 82°$. Since these levels are coupled by the off-diagonal matrix elements $\langle \pm\frac{1}{2}, 1, 0 \mid \mathcal{H}_{\mathrm{ESR}} \mid \pm\frac{1}{2}, \frac{1}{4}, -1\rangle$, they repel each other near 82°, and consequently the ESR lines do also. The closeness of approach and the sharpness of the repulsion are determined by the size of the coupling matrix element.

The magnitude of $\langle \pm\frac{1}{2}, 1, 0 \mid \mathcal{H}_{\mathrm{ESR}} \mid \pm\frac{1}{2}, 1, -1\rangle$ for the V_{KA} center where $T_\perp\approx 0$ G is considerably smaller than that for the typical V_K center, where $T_\perp\approx 50$ G. This accounts for the the difference in the repulsion between the R_2 and R_4 lines evident in the calculated curves of the V_K center and V_{KA} center in Fig. 3. Both $M=0$ lines of the V_{KA} center are involved in the

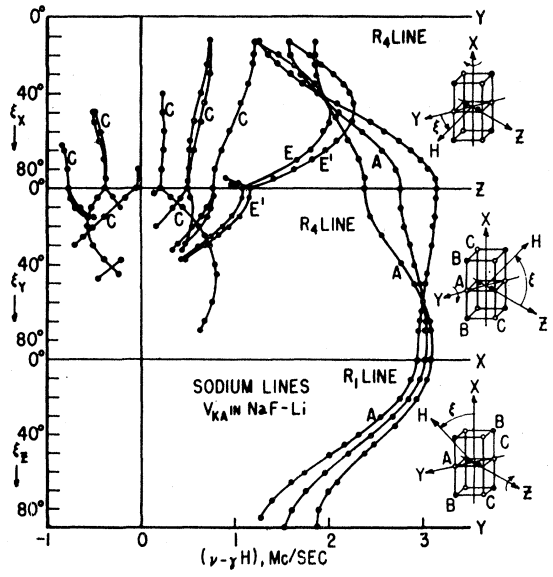

FIG. 8. ENDOR angular dependence of sodium lines of the lithium V_{KA} center in NaF.

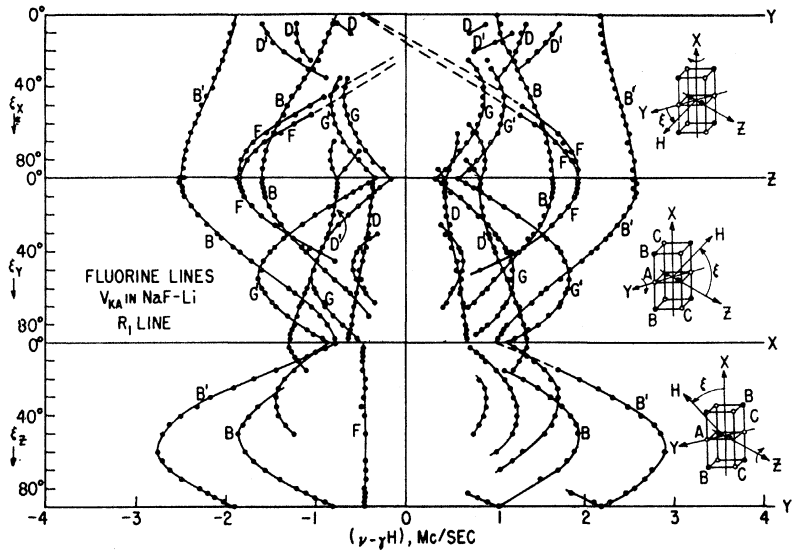

FIG. 9. ENDOR angular dependence of fluorine lines of lithium V_{KA} center in NaF.

repulsion because these states have been mixed by the bent bond (the singlet of the V_K center is "pure"). The overlap of ESR lines mentioned previously prevented direct observation of the sharp bends predicted for the V_{KA} center at 82°. In fact, the experimental point at 77.5° taken on the R_4 line possibly indicates that the bends are not as sharp as predicted. One final point in this connection is that the R_2 line for $\zeta > 85°$ becomes associated with the $M=-1$ nuclear state, while the R_4 line becomes associated with the $M=0$ state (both $M=0$ states for the V_{KA} center, but only the $M=0$ component of the triplet for the V_K center). However, for ζ very close to 90°, the $M=\pm 1$ nuclear states are nearly degenerate, so that the states which produce the R_1 and R_2 lines are almost equal mixtures of the two nuclear states.

IV. ENDOR SPECTRUM

A. Verification of Model

The ENDOR spectrum of the lithium V_{KA} center in NaF provided definite confirmation of the model illustrated in Fig. 1. ENDOR lines were identified for

TABLE IV. Principal-axis (x, y, z) hyperfine values in Mc/sec and orientations (α, β, γ) with respect to the molecule-ion principal axes (X, Y, Z) for all observed nuclei (except E, E', G', and G) of the lithium V_{KA} center in NaF and some nuclei of the V_K centers in NaF and LiF.

Center	Nucleus	A_x (Mc/sec)	A_y (Mc/sec)	A_z (Mc/sec)	α	β	γ
Li V_{KA}	A(Na)	−6.15±0.04	−3.17±0.04	−5.50±0.04	0°	0°	0°
V_K[a]	A(Na)	−7.15	−4.10	−6.36	0°	0°	0°
Li V_{KA}	A′(Li)	−6.04±0.02	+1.65±0.02	−4.06±0.02	0°	0°	0°
V_K[b] (LiF)	A(Li)	−7.95	+0.97	−5.36	0°	0°	0°
Li V_{KA}	B(F)	+1.34±0.06	−3.945±0.02	−3.22±0.02	38.7±0.5°	38.7±0.5°	0°
V_K[a]	B(F)	+0.85	−4.57	−3.74	36°	36°	0°
Li V_{KA}	B′(F)	−0.22±0.06	−5.85±0.02	−5.01±0.02	32.2±0.5°	32.2±0.5°	0°
Li V_{KA}	C(Na)	+2.20±0.50	−1.55±0.10	−1.10±0.10	≈15°	≈7.5°	≈15°
Li V_{KA}	D(F)	−1.36±0.02	+2.52±0.08	−1.10±0.04	0°	16.3±1.5°	16.3±1.5°
V_K[a]	D(F)	−1.56	+3.05	−1.22	0°	16°	16°
Li V_{KA}	D′(F)	−2.77±0.02	+3.35±0.08	−1.73±0.04	0°	10±2°	10±2°
Li V_{KA}	F(F)	−1.06±0.04	−1.06±0.04	+3.77±0.02	0°	2.5±0.5°	2.5±0.5°
V_K[a]	F(F)	−1.10	−1.10	+3.95	0°	0°	0°

[a] Reference 10, [b] References 5, 8, and 9.

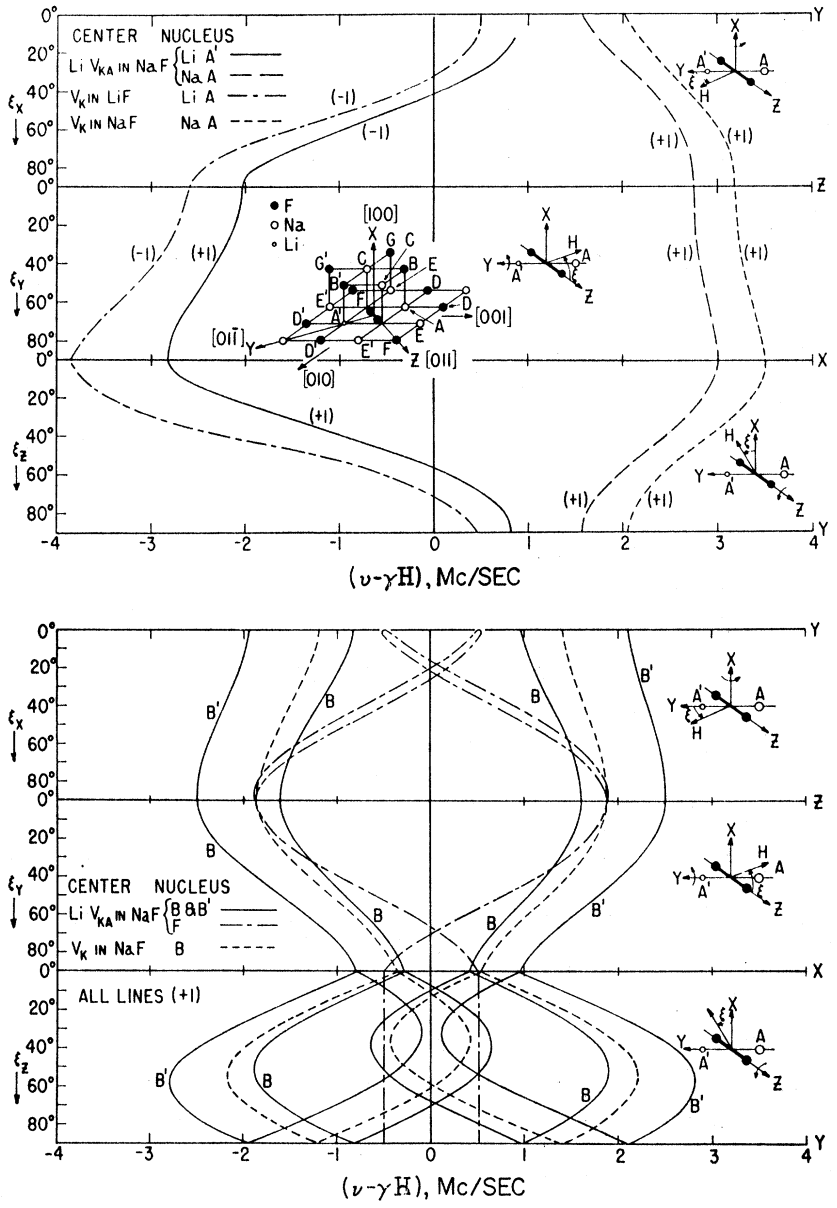

FIG. 10. Comparison of the angular dependence of some ENDOR lines of the lithium V_{KA} center in NaF with corresponding lines of the V_K centers in NaF and LiF. For clarity only the central line of a quadrupole triplet is shown for the sodium lines.

the nuclei labeled A, A′, B, B′, C, D, D′, E, E′, F, G, and G′ in the figure. A typical ENDOR spectrum is shown in Fig. 7. In each instance the angular dependence was consistent with the symmetries of the model. Some experimental angular dependence curves are given in Figs. 8 and 9 and the hyperfine constants are tabulated in Table IV.

The data were taken using the same procedures as in the ENDOR studies of the V_K centers in NaF [10] and LiF,[8,9] and the format of presentation of the angular dependences is the same as in Refs. 8–10. The three panels of a typical figure correspond to rotations of the magnetic field about the X, Y, and Z axes (see Fig. 1), and the frequencies on the horizontal axis are the hyperfine shifts, $\nu-\gamma H$, where ν is the observed ENDOR frequency, γ is the nuclear gyromagnetic ratio, and H is the magnetic field.

Except for a small portion of the lithium A′ angular dependence taken on the R_2 and R_3 ESR lines, the ENDOR data were limited to the R_1 line and to the R_4 line in regions where it is resolved from the superposition of ESR lines at the center of the spectrum. Optical orientation of the V_K centers in NaF [10] and LiF [8,9] permitted observation of reasonably complete angular dependences on the R_2 and R_3 lines. Instead of selectively orienting the V_{KA} centers, these methods disassociated the self-trapped holes from the lithium ions.

Because the perturbation of the unpaired electron wave function by the impurity in the V_{KA} center is small, there is a close resemblance between the angular

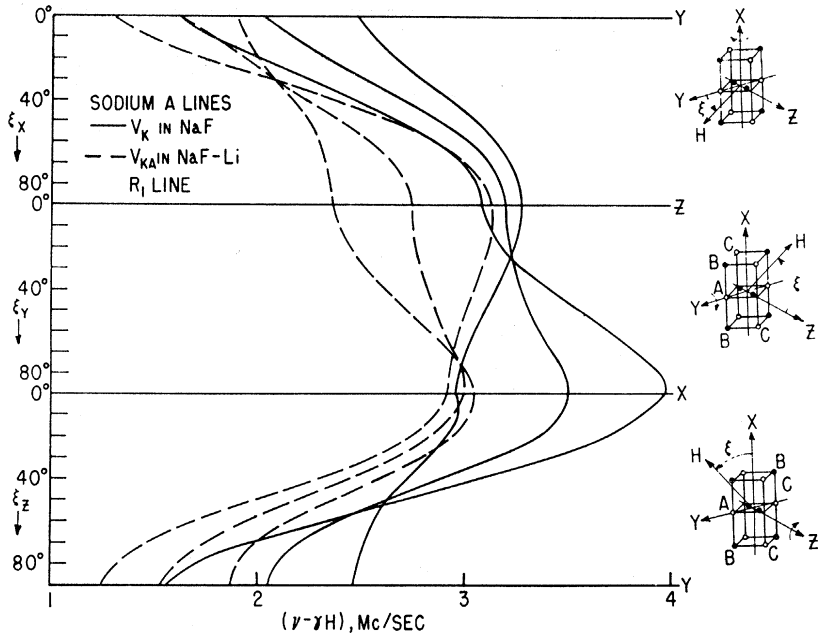

FIG. 11. Comparison of the ENDOR angular dependence of the sodium A nucleus of the lithium V_{KA} center with the sodium A nucleus of the V_K center in NaF.

dependences of nuclei of the same type which occupy corresponding lattice sites in the V_{KA} and V_K centers. This similarity greatly facilitated the identification of ENDOR lines of the V_{KA} center and is illustrated in Figs. 10 and 11, where the angular dependences of some nuclei of the V_{KA} and V_K centers are compared.

Symmetry arguments like those used in the V_K center studies[8–10] were also used here to verify consistency with the model and to identify ENDOR lines. The V_K center and the V_{KA} center both have reflection symmetry through the XY and YZ planes (Fig. 1), but only the V_K center has reflection symmetry through the XZ plane also. As a consequence, nuclei which occupy lattice sites exchanged by reflection through the XZ plane may be equivalent for certain field orientations in the V_K center but are always nonequivalent in the V_{KA} center (distinguished by primed and unprimed letters). Furthermore, nuclei which occupy lattice sites contained in the XZ plane have the Y axis as a principal axis in the V_K center but do not in the V_{KA} center. These are the basic qualitative differences between the ENDOR spectra of the V_K and V_{KA} centers. Experimental observations of these differences include the identification of the ENDOR lines of the B, B′, D, D′, E, E′, G and G′ nuclei of the V_{KA} center (Figs. 8 and 9), and the splitting of the ENDOR lines of the C and F nuclei of the V_{KA} center for magnetic field rotation in the YZ plane.

In Fig. 1 we have labeled the nuclei on the same side of the XZ plane as the sodium A nucleus with the unprimed letters B, D, E, and G, and those on the lithium A′ side of the XZ plane with the primed letters B′, D′, E′, and G′. However, there is no unique way of correlating the experimental data with the primed and unprimed lattice sites.

The angular dependence curves of the B nuclei of the V_K center in Fig. 10 are seen to fall between the curves of the B and B′ nuclei of the V_{KA} center. The V_K center curve is closer to the V_{KA} center curve with the smaller hyperfine constants. The local environment of the unprimed nuclei resembles that of the corresponding nuclei of the V_K center more than that of the unprimed nuclei. This suggests that we identify the B nuclei with the V_{KA} center ENDOR lines closest to the corresponding V_K center lines. Similar relations between the ENDOR lines occur for the primed and unprimed D, E, and G nuclei.

The Fermi contact interaction is proportional to the unpaired spin density at a nuclear site and is given by one-third the sum of the three principal values of the nuclear hyperfine tensor. From the values of Table IV we may compare the contact interactions of the B, B′, and B_K nuclei. According to the proposed assignment, the B′ nuclei have the largest and the B nuclei have the smallest contact interaction and the value for the V_K center B nuclei falls between these but is closer to that of the unprimed B nuclei. These relative magnitudes suggest that the primed nuclei and the F_2^- molecule ion move toward each other by partial relaxation into the lattice site of the small Li^+ ion. Strong support for this interpretation is the fact that the contact interaction of the sodium A nucleus is less than that of the sodium A_K nuclei. This is the one instance where the V_{KA} center nucleus is known to be on a particular side of the XZ plane and thus permits an unambiguous comparison with the corresponding nuclei of the V_K center.

B. Quantitative Analysis

The frequency ν and the hyperfine shifts $\nu-\gamma H$ of ENDOR transitions for nuclei neighboring the V_{KA} center were calculated with the following effective spin

Hamiltonian (in Mc/sec):

$$\mathcal{H}=\mathcal{H}_{\mathrm{ESR}}+\mathbf{I}\cdot\mathbf{A}\cdot\mathbf{S}-\gamma_n\mathbf{H}_0\cdot\mathbf{I}, \qquad (10)$$

where $\mathbf{I}$ is the nuclear-spin operator, $\mathbf{A}$ is the nuclear hyperfine tensor (in Mc/sec), γ_n is the nuclear gyromagnetic ratio (in Mc/sec G), and $\mathcal{H}_{\mathrm{ESR}}$ is given by Eqs. (1) and (7). The experimental angular dependences were used to determine the principal values and the principal axes orientations of the hyperfine tensor $\mathbf{A}$ for the A, A′, B, B′, C, D, D′, and F nuclei (Table IV). Although well-resolved quadrupole triplets were observed for the sodium nuclei, the splitting for the A and C nuclei is sufficiently small to permit the accurate calculation of the hyperfine constants with Eq. (10) if the central line $(+\frac{1}{2}\rightarrow-\frac{1}{2})$ of the triplet is used. No hyperfine constants for the sodium E and E′ nuclei were calculated because the central line $(+\frac{1}{2}\rightarrow-\frac{1}{2})$ could not be identified. The quadrupole triplet splitting of the lithium A′ nucleus is barely resolvable. Thus, the spin Hamiltonian of Eq. (10) without a nuclear quadrupole term is adequate for the calculation of those hyperfine constants given in Table IV. Calculation methods were only developed for nuclei with at least one of the principal hyperfine axes parallel to one of the three axes X, Y, and Z (Fig. 1). No hyperfine constants were calculated for the G and G′ nuclei because they do not satisfy this requirement (see Ref. 10 for a discussion of the G nuclei for the V_K center). Although the C nuclei also do not satisfy this requirement, one of their principal axes is nearly parallel to the Y axis (differs by $7.5°\pm2°$). The principal hyperfine values of the C nuclei were calculated by assuming that the two axes coincide and the error thus introduced is more than covered by the comparatively large uncertainty given.

The calculations consist of finding the eigenvalues of the spin Hamiltonian in Eq. (10) from which the frequencies of the allowed ENDOR transitions ($|\Delta m_I|=1$, $\Delta m_s=\Delta m=0$) can be calculated directly. The experimental parameters g_X, g_Y, g_Z, T_x, T_y, T_z and δ of the ESR part of the Hamiltonian are fixed at the values given in Table I, and the hyperfine constants of A are adjusted to produce agreement between the calculated and experimental angular dependence. In the ENDOR study of the V_K center in LiF, Gazzinelli and Mieher[9] developed perturbation methods for this calculation. For the $M=0$ ESR lines the hyperfine interaction of the molecular fluorines can be neglected, and their perturbation calculation is patterned after one described by Slichter (Chap. 7).[5] Since very little ENDOR data for the V_{KA} center was obtained from the $M=0$ lines, this method could not be used to determine hyperfine constants. For the $M=\pm1$ ESR lines, the ENDOR frequencies are strongly perturbed by the molecular fluorine hyperfine interaction. The perturbation calculations of Gazzinelli and Mieher for $M=\pm1$ were adequate for the angle $\zeta<\approx75°$ (see Fig. 2), but they break down in the range $75°<\zeta\leq90°$. Therefore, this method could not be used to make accurate calculations

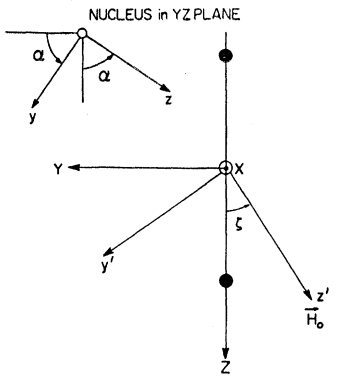

FIG. 12. The orientation of the principal axes, y and z, of the hyperfine tensor of a typical ENDOR nucleus in the YZ plane.

of principal hyperfine values for principal axes making an angle greater than 75° with the molecular axis.

In order to obtain hyperfine constants whose accuracy is only limited by experimental uncertainties, the matrix of the spin Hamiltonian in Eq. (10) was diagonalized numerically on an IBM 7090 computer. The smallest experimental error is the ≈10 kc/sec uncertainty in the measurement of the frequency of an ENDOR line (typical linewidth ≈50 kc/sec). The numerical accuracy of the computer program is well within this limit for the matrices encountered.

The form of the spin Hamiltonian matrix differed depending on the orientation of the principal hyperfine axes and the field rotation plane. To illustrate the calculation of the matrix, consider a nucleus with one principal axis parallel to the X axis (any nucleus contained in the YZ plane) and field rotation in the YZ plane. The appropriate geometric parameters are specified in Fig. 12. The quantization direction and representations of the spin operators $\mathbf{S}$, $\mathbf{K}^+$, and $\mathbf{K}^-$ are those used in the ESR calculations [Eqs. (2) and (3)]. The nuclear spin $\mathbf{I}$ is quantized along the magnetic field for the purpose of specifying its zeroth-order spin function. Since, as mentioned previously, nuclear quadrupole effects can be neglected, we may take the value of the nuclear spin I to be $\frac{1}{2}$. Consequently, the zeroth-order nuclear spin function is $|m_I\rangle$, where $m_I=\pm\frac{1}{2}$ is the projection of $\mathbf{I}$ along $\mathbf{H}_0$. The quantum number I is redundant and has been dropped. The 16 basic spin functions used to calculate the spin Hamiltonian matrix are taken to be the product states

$$|m_s, K^+, M\rangle\,|m_I\rangle=|m_s, K^+, M, m_I\rangle, \qquad (11)$$

where $|m_s, K^+, M\rangle$ is given by Eqs. (2) and (3).

In this representation the ENDOR part of the total spin Hamiltonian [Eq. (10)],

$$\mathcal{H}_{\mathrm{ENDOR}}=\mathbf{I}\cdot\mathbf{A}\cdot\mathbf{S}-\gamma_n\mathbf{H}_0\cdot\mathbf{I}, \qquad (12)$$

is expanded with the components of $\mathbf{I}$ and $\mathbf{S}$ expressed in the $x'y'z'$ coordinate system, and $\mathcal{H}_{\mathrm{ESR}}$ is expanded as

TABLE V. The matrix $\langle m_s, K^+, M, m_I \mid \mathcal{H}_{\mathrm{ESR}}+\mathcal{H}_{\mathrm{ENDOR}} \mid$

$\mid 1a\rangle$	$\mid 1b\rangle$	$\mid 2a\rangle$	$\mid 2b\rangle$	$\mid 3a\rangle$	$\mid 3b\rangle$	$\mid 4a\rangle$	$\mid 4b\rangle$
$W+W_{zz}+V_{11}$	W_{yz}	V_{12}	0	0	0	V_{14}	0
	$-W-W_{zz}+V_{11}$	0	V_{12}	0	0	0	V_{14}
		$W+W_{zz}+V_{22}$	W_{yz}	V_{12}	0	V_{24}	0
			$-W-W_{zz}+V_{22}$	0	V_{12}	0	V_{24}
				$W+W_{zz}+V_{33}$	W_{yz}	V_{34}	0
					$-W-W_{zz}+V_{33}$	0	V_{34}
						$W+W_{zz}+V_{44}$	W_{yz}
							$-W-W_{zz}+V_{44}$

in the ESR calculations [Eqs. (4)–(7)]. We write

$$\mathcal{H}_{\mathrm{ENDOR}}=-\gamma_n H_0 I_z+A_x I_x S_x+A_y I_y S_y+A_z I_z S_z, \quad (13)$$

where A_x, A_y, and A_z are the principal values of **A**. Through the transformations

$$I_{xyz}=R(-\theta)I_{x'y'z'},$$
$$S_{xyz}=R(-\theta)S_{x'y'z'}, \quad (14)$$

where $\theta=\zeta-\alpha$ and $R(-\theta)$ is given by Eq. (5), Eq. (13) takes the form

$$\begin{aligned}\mathcal{H}_{\mathrm{ENDOR}}=&-\gamma_n H_0 I_{z'}+A_x I_{x'} S_{x'}\\&+(A_y\cos^2\theta+A_z\sin^2\theta)I_{y'}S_{y'}\\&+(A_z-A_y)(\sin\theta\cos\theta)I_{y'}S_{z'}\\&+(A_z-A_y)(\sin\theta\cos\theta)I_{z'}S_{y'}\\&+(A_y\sin^2\theta+A_z\cos^2\theta)I_{z'}S_{z'}. \quad (15)\end{aligned}$$

The matrix $\langle m_s, K^+, M, m_I \mid \mathcal{H} \mid m_s', K^{+\prime}, M', m_I'\rangle$, where $\mathcal{H}=\mathcal{H}_{\mathrm{ESR}}+\mathcal{H}_{\mathrm{ENDOR}}$, is given in Table V. The states $\langle m_s, K^+, M \mid$ are the same as in Eq. (8) and the m_I states are represented by $\langle a \mid$ for $m_I=+\frac{1}{2}$ and $\langle b \mid$ for $m_I=-\frac{1}{2}$. For example, a typical state is

$$\langle m_s, K^+, M, m_I \mid =\langle \tfrac{1}{2}, 1, 0, -\tfrac{1}{2} \mid =\langle 2b \mid .$$

The terms in Table V are

$$\begin{aligned}W&=-\tfrac{1}{2}\gamma_n H_0,\\W_{zz}&=\tfrac{1}{4}(A_y\sin^2\theta+A_z\cos^2\theta),\\W_{yy}&=\tfrac{1}{4}(A_y\cos^2\theta+A_y\sin^2\theta),\\W_{xx}&=\tfrac{1}{4}A_x,\\W_{yz}&=\tfrac{1}{4}(A_z-A_y)(\sin\theta\cos\theta), \quad (16)\end{aligned}$$

and $V_{ij}=ij$th matrix element of Table II. Again all terms are chosen so that the matrix is in units of Mc/sec.

When calculating the corresponding spin Hamiltonian matrix for the other field rotations and orientations of the principal hyperfine axes which occurred, **S** and **I** were always quantized along the field and $\mathbf{K}^+$ and $\mathbf{K}^-$ along the molecular axis as was done in the ESR analysis. Similar submatrices for the spin operator components were also used (see the Appendix). When $\mathbf{H}_0$ was not in a principal plane the matrix contained complex matrix elements. The eigenvalues of a complex Hermitian matrix, $A+iB$, where A and B are real

m_s', $K^{+\prime}$, M', m_I'). The terms W_{ij} and V_{ij} are given in Eq. (16).

$\|5a\rangle$	$\|5b\rangle$	$\|6a\rangle$	$\|6b\rangle$	$\|7a\rangle$	$\|7b\rangle$	$\|8a\rangle$	$\|8b\rangle$	
$W_{yz}+V_{15}$	$-W_{xx}+W_{yy}$	V_{16}	0	0	0	V_{18}	0	$\langle 1a\|$
$W_{xx}+W_{yy}$	$-W_{yz}+V_{15}$	0	V_{16}	0	0	0	V_{18}	$\langle 1b\|$
V_{25}	0	$W_{yz}+V_{26}$	$-W_{xx}+W_{yy}$	V_{16}	0	V_{28}	0	$\langle 2a\|$
0	V_{25}	$W_{xx}+W_{yy}$	$-W_{yz}+V_{26}$	0	V_{16}	0	V_{28}	$\langle 2b\|$
0	0	V_{25}	0	$W_{yz}+V_{37}$	$-W_{xx}+W_{yy}$	V_{38}	0	$\langle 3a\|$
0	0	0	V_{25}	$W_{xx}+W_{yy}$	$-W_{yz}+V_{37}$	0	V_{38}	$\langle 3b\|$
V_{25}	0	V_{46}	0	V_{47}	0	$W_{yz}+V_{48}$	$-W_{xx}+W_{yy}$	$\langle 4a\|$
0	V_{45}	0	V_{46}	0	V_{47}	$W_{xx}+W_{yy}$	$-W_{yz}+V_{48}$	$\langle 4b\|$
$W-W_{zz}+V_{55}$	$-W_{yz}$	V_{56}	0	0	0	V_{58}	0	$\langle 5a\|$
	$-W+W_{zz}+V_{55}$	0	V_{56}	0	0	0	V_{58}	$\langle 5b\|$
		$W-W_{zz}+V_{66}$	$-W_{yz}$	V_{56}	0	V_{68}	0	$\langle 6a\|$
			$-W-W_{zz}+V_{66}$	0	V_{56}	0	V_{68}	$\langle 6b\|$
				$W-W_{zz}+V_{77}$	$-W_{yz}$	V_{78}	0	$\langle 7a\|$
					$-W+W_{zz}+V_{77}$	0	V_{78}	$\langle 7b\|$
						$W-W_{zz}+V_{88}$	$-W_{yz}$	$\langle 8a\|$
							$-W+W_{zz}+V_{88}$	$\langle 8b\|$

matrices, are idential with the twofold degenerate eigenvalues of the real symmetric matrix

$$\begin{pmatrix} A & B \\ B & A \end{pmatrix}.$$

Therefore, although the diagonalization subroutine used was applicable to real symmetric matrices only, it could be adapted readily to calculating the eigenvalues of the complex Hermitian matrices encountered.

C. Comparison of Theory and Experiment

Typical comparisons between calculated and experimental angular dependences are given in Figs. 13–15 for the sodium A, the lithium A′, and the fluorine B′ nuclei, respectively. The experimental points represented by circles and triangles in these figures constitute the data from which ENDOR lines were identified and were the first data taken. Discrepancies between these points and the calculated curves are in many instances several times greater than the 10-kc/sec minimum experimental uncertainty. These errors were due to a time-constant shift resulting from sweeping through an ENDOR line too rapidly. It was not feasible to take all of the data while sweeping frequency slowly enough to reduce the time-constant shift to less than 10 kc/sec. Instead, certain experimental points were remeasured accurately by sweeping through the ENDOR lines stepwise and reading the cycle counter dirctly at each step. These points are indicated by crosses in the figures. They were selected to give the most accurate determination of hyperfine constants and to provide a comparison with calculations in the regions of greatest interest ($75°<\zeta\leq 90°$). The time-constant shifted data are also included to give a picture of the over-all comparison between calculations and experiment. The agreement for the carefully measured points is within 10 kc/sec, and the other experimental points indicate that this close agreement should hold for the entire angular dependence.

The present calculations describe (within 10 kc/sec) the observed angular dependences in the regions where the angle between the magnetic field and the molecular axis is greater than $\approx 75°$, while the perturbation theory[9] fails to do so. This is best illustrated by the angular dependence of the lithium A′ nucleus in Fig. 14, where calculations are given for all and observations for at least three of the ESR lines in the region of interest ($75°<\xi_y\leq 90°$). The lithium A′ ENDOR lines were observed on the R_3 and R_4 ESR lines for $82°<\xi_y\leq 90°$ even though these ESR lines are not resolved from the ESR lines of other orientations of V_{KA} centers. This was possible because these ENDOR lines are well separated from any other ENDOR lines. The magnetic field was adjusted near the expected value until they were observed. However, it was not possible to distinguish between the R_3 and R_4 ESR lines by this method.

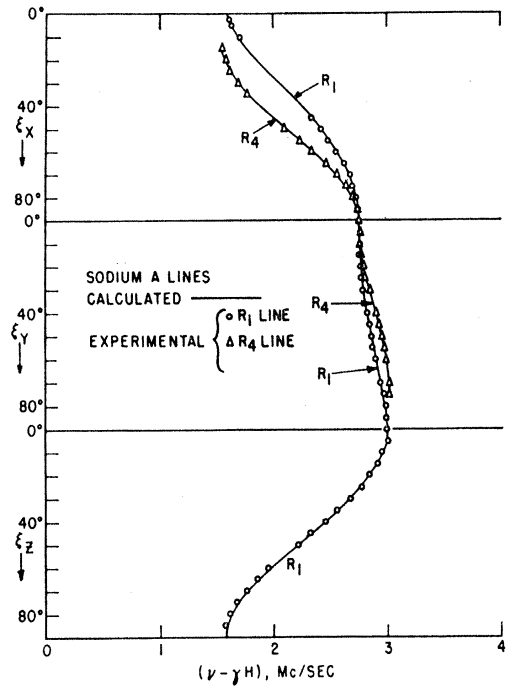

FIG. 13. Comparison of a calculated and experimental ENDOR angular dependence for the sodium A nucleus for the R_1 and R_4 ESR lines of the V_{KA} center.

Several features of the spectrum at $\xi_y=90°$ were found to hold generally for the 90° spectrum (H_0 perpendicular to the molecular axis) of all nuclei as predicted by the matrix diagonalization calculations. These are

(a) The R_1 and R_2 ENDOR lines (the ENDOR spectrum or lines observed on the R_i ESR line, $i=1, 2, 3, 4$, are designated the R_i ENDOR spectrum or lines) have the same values of $\nu-\gamma H$, and the R_3 and R_4 ENDOR lines have the same values of $\nu-\gamma H$.

(b) The R_1 and R_2 ENDOR lines are generally, but not always resolvably shifted from the R_3 and R_4 ENDOR lines, and by amounts which generally differ for the two m_s states ($\pm\frac{1}{2}$).

(c) The position of the R_3 and R_4 ENDOR lines is that predicted by the simplest calculations which do not include the perturbations caused by the molecular fluorine hyperfine interaction.

These predictions were verified in greater detail for the lithium A′ nucleus than for other nuclei where data was limited to the R_1 line, but in all cases the agreement was within experimental error. In contrast, the perturbation calculations[9] predict that all four ENDOR lines (R_1, R_2, R_3, and R_4) occur at the position of the R_3 and R_4 lines when H_0 is perpendicular to the molecular axis.

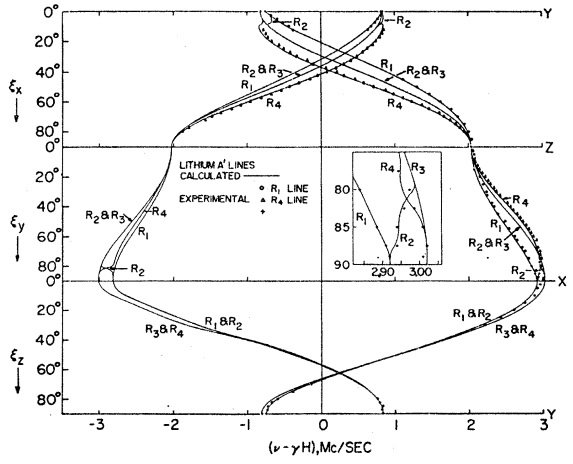

FIG. 14. Comparison of calculated and experimental ENDOR angular dependence of the lithium A′ nucleus for different ESR lines. The crosses indicate carefully measured points.

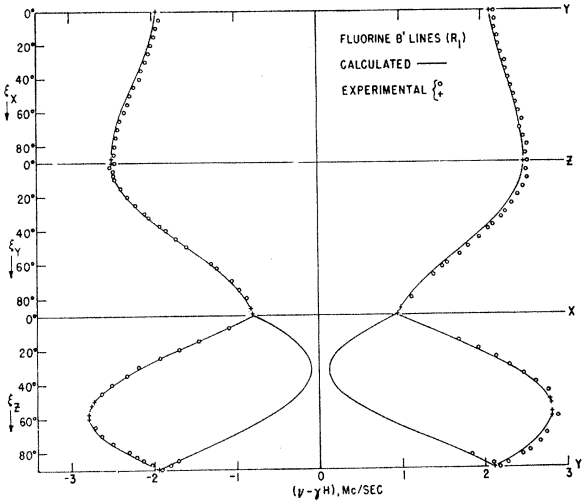

FIG. 15. Comparison of calculated and experimental ENDOR angular dependence of the fluorine B′ nuclei for the R_1 ESR line. The crosses indicate carefully measured points.

The shifts of ENDOR lines caused by the molecular fluorine hyperfine interaction can now be summarized by several statements which apply generally for all orientations of magnetic field. First, these shifts only occur on ESR lines produced by the $M=\pm1$ molecular fluorine spin states or by linear combinations of these states. These include the R_1 and R_4 lines for $\zeta<81°$, and the R_1 and R_2 lines for $\zeta>83°$. Second, these shifts are caused by the perturbations of the matrix elements

$$\langle \tfrac{1}{2}, 1, \pm1, m_I \,|\, \mathcal{H} \,|\, -\tfrac{1}{2}, 1, \pm1, m_I \rangle$$

which mix the two electron spin states $m_s=\pm\frac{1}{2}$. In the matrix of Table V, the magnitude of these matrix elements varies approximately as $T_z \sin\zeta$ and ranges from zero at $\zeta=0°$ to $\approx$1300 Mc/sec at $\zeta=90°$. Third, the behavior of the calculated ENDOR angular de-

pendences as ζ passes through 82° can be described in terms of antilevel crossings as was done for the ESR angular dependence in Sec. III. Namely, the R_2 ENDOR line for $\zeta>82°$ is the continuation of the R_4 ENDOR line for $\zeta<82°$, etc. Finally, the calculations show that the effect of the bent bond on the ENDOR frequencies is less than the 10-kc/sec minimum experimental uncertainty. (Exceptions to this occurred on the R_2, R_3, and R_4 ESR lines for field orientations in the narrow range $81°<\zeta<83°$, but no data were taken in these regions as mentioned in Sec. III.) Although the bent-bond angle δ is important in determining the position of the two ESR lines corresponding to the $M=0$ molecular flourine spin states, the shifts for $\nu-\gamma H$ values of the ENDOR lines do not occur for the $M=0$ states. Therefore, sufficiently accurate ENDOR hyperfine constants could have been calculated for the V_{KA} center without including the bent-bond terms in Table V.

V. CONCLUSION

A new ESR center consisting of a self-trapped hole associated with an alkali impurity has been discovered. The model has been verified by an ENDOR study of the system in crystals of NaF containing Li^+ ion impurities. All of the details of the ESR and ENDOR experimental angular dependences can be explained theoretically by diagonalization of the complete spin Hamiltonian.

APPENDIX

To obtain the matrix $\langle m_s, K^+, M \mid \mathcal{H}_{\mathrm{ESR}} \mid m_s', K^{+\prime}, M' \rangle$ as given by Table II and Eq. (9) we need the submatrices of $S_{x'}$, $S_{y'}$, $S_{z'}$ for the states $m_s=\pm\frac{1}{2}$ and the submatrices of K_x^+, K_y^+, K_z^+, K_x^-, K_y^-, K_z^- for the states $K^+=1$, $M=\pm1, 0$ and $K^+=0$, $M=0$. These are chosen to be

$$S_j=\begin{vmatrix} \langle \frac{1}{2} \mid S_j \mid \frac{1}{2}\rangle & \langle \frac{1}{2} \mid S_j \mid -\frac{1}{2}\rangle \\ \langle -\frac{1}{2} \mid S_j \mid \frac{1}{2}\rangle & \langle -\frac{1}{2} \mid S_j \mid -\frac{1}{2}\rangle \end{vmatrix}, \quad 2S_{x'}=\begin{vmatrix} 0 & i \\ -i & 0 \end{vmatrix}, \quad 2S_{z'}=\begin{vmatrix} 0 & 1 \\ 1 & 0 \end{vmatrix}, \quad 2S_{z'}=\begin{vmatrix} 1 & 0 \\ 0 & 1 \end{vmatrix};$$

$$\langle K_j^{\pm}\rangle=\begin{vmatrix} \langle 1,1 \mid K_j^{\pm} \mid 1,1\rangle & \langle 1,1 \mid K_j^{\pm} \mid 1,0\rangle & \langle 1,1 \mid K_j^{\pm} \mid 1,-1\rangle & \langle 1,1 \mid K_j^{\pm} \mid 0,0\rangle \\ \langle 1,0 \mid K_j^{\pm} \mid 1,1\rangle & \langle 1,0 \mid K_j^{\pm} \mid 1,0\rangle & \langle 1,0 \mid K_j^{\pm} \mid 1,-1\rangle & \langle 1,0 \mid K_j^{\pm} \mid 0,0\rangle \\ \langle 1,-1 \mid K_j^{\pm} \mid 1,1\rangle & \langle 1,-1 \mid K_j^{\pm} \mid 1,0\rangle & \langle 1,-1 \mid K_j^{\pm} \mid 1,-1\rangle & \langle 1,-1 \mid K_j^{\pm} \mid 0,0\rangle \\ \langle 0,0 \mid K_j^{\pm} \mid 1,1\rangle & \langle 0,0 \mid K_j^{\pm} \mid 1,0\rangle & \langle 0,0 \mid K_j^{\pm} \mid 1,-1\rangle & \langle 0,0 \mid K_j^{\pm} \mid 0,0\rangle \end{vmatrix}, \quad (j=x,y,z)$$

$$\langle K_x^+\rangle=\begin{vmatrix} 0 & i/\sqrt{2} & 0 & 0 \\ -i/\sqrt{2} & 0 & i/\sqrt{2} & 0 \\ 0 & -i/\sqrt{2} & 0 & 0 \\ 0 & 0 & 0 & 0 \end{vmatrix}, \quad \langle K_y^+\rangle=\begin{vmatrix} 0 & \frac{1}{2}\sqrt{2} & 0 & 0 \\ \frac{1}{2}\sqrt{2} & 0 & \frac{1}{2}\sqrt{2} & 0 \\ 0 & \frac{1}{2}\sqrt{2} & 0 & 0 \\ 0 & 0 & 0 & 0 \end{vmatrix}, \quad \langle K_z^+\rangle=\begin{vmatrix} 1 & 0 & 0 & 0 \\ 0 & 0 & 0 & 0 \\ 0 & 0 & -1 & 0 \\ 0 & 0 & 0 & 0 \end{vmatrix},$$

$$\langle K_x^-\rangle=\begin{vmatrix} 0 & 0 & 0 & -i/\sqrt{2} \\ 0 & 0 & 0 & 0 \\ 0 & 0 & 0 & -i/\sqrt{2} \\ i/\sqrt{2} & 0 & i/\sqrt{2} & 0 \end{vmatrix}, \quad \langle K_y^-\rangle=\begin{vmatrix} 0 & 0 & 0 & -\frac{1}{2}\sqrt{2} \\ 0 & 0 & 0 & 0 \\ 0 & 0 & 0 & \frac{1}{2}\sqrt{2} \\ -\frac{1}{2}\sqrt{2} & 0 & \frac{1}{2}\sqrt{2} & 0 \end{vmatrix}, \quad \langle K_z^-\rangle=\begin{vmatrix} 0 & 0 & 0 & 0 \\ 0 & 0 & 0 & 1 \\ 0 & 0 & 0 & 0 \\ 0 & 1 & 0 & 0 \end{vmatrix}.$$

The matrices of the components of K^+ and K^- are easily computed by using the expression for the total spin wave function in Eq. (3). The matrices for the components of K_1 and K_2 in Eq. (3) are chosen to be the same as those for the respective components of S above.[12]

The matrices for $S_{x'}$ and $S_{y'}$ differ from the standard choice by a phase factor that is equivalent to a rotation of 90° about the z' axis. This choice was made because most of the analysis was done for the magnetic field in the plane of the bent bond which had been chosen in earlier work to be the YZ principal plane. The above choice of $S_{y'}$ results in real matrix elements for the YZ plane rotation work.